scientific reports

Check for updates

OPEN

# Control of monomeric Vo's versus Vo clusters in $ZrO_{2-x}$ for solar-light $H_2$ production from $H_2O$ at high-yield (millimoles $gr^{-1}$ $h^{-1}$)

Yiannis Deligiannakis[1,4]✉, Asterios Mantzanis[1], Areti Zindrou[1], Szymon Smykala[3] & Maria Solakidou[1,2]

**Pristine zirconia, $ZrO_2$, possesses high premise as photocatalyst due to its conduction band energy edge. However, its high energy-gap is prohibitive for photoactivation by solar-light. Currently, it is unclear how solar-active zirconia can be designed to meet the requirements for high photocatalytic performance. Moreover, transferring this design to an industrial-scale process is a forward-looking route. Herein, we have developed a novel Flame Spray Pyrolysis process for generating solar-light active nano-$ZrO_{2-x}$ via engineering of lattice vacancies, Vo. Using solar photons, our optimal nano-$ZrO_{2-x}$ can achieve milestone $H_2$-production yield, > 2400 μmol$g^{-1}$ $h^{-1}$ (closest thus, so far, to high photocatalytic water splitting performance benchmarks). Visible light can be also exploited by nano-$ZrO_{2-x}$ at a high yield via a two-photon process. Control of monomeric Vo versus clusters of Vo's is the key parameter toward Highly-Performing-Photocatalytic $ZrO_{2-x}$. Thus, the reusable and sustainable $ZrO_{2-x}$ catalyst achieves so far unattainable solar activated photocatalysis, under large scale production.**

Sunlight energy storage to $H_2$ via photocatalytic water splitting[1,2] bears key advantages, such as high energy-storage capacity of $H_2$ 141.6 kJ $g^{-1}$ versus 0.46–0.72 kJ $g^{-1}$ on Li-batteries[3]. Water photocatalysis to produce $H_2$ is an inherently green-technology, fully compliant with circular economy[4]. Moreover, maximization of photocatalytic efficiency *in tandem* with minimized costs for industrial-scale production is mandatory. So far, most literature reports on high-performance photocatalysts (HPP) refer to nanomaterials with focus on performance optimization[5]. Except $TiO_2$, industrial-scale and cost-effective production of HPP's remains at its infancy.

Metal oxides can be HPP's as long as they fulfill certain key criteria: $H_2$ production and $CO_2$ reduction, are favored by high conduction band (CB) semiconductors. Pristine zirconia ($ZrO_2$) has one of the highest CB-edge energies among metal oxides $E_{CB} = -1100$ mV versus NHE. However, its band-gap energy $E_g > 5$ eV requires highly energetic photons, i.e., $\lambda < 225$ nm, which is prohibitive for solar-light harvesting. In this context, pristine $ZrO_2$ despite its established uses in technology, e.g. as refracting coating[6], thermal coating[7], gas-sensing[8], fuel cells[9], Water–Gas-Shift reaction[10], so far, has not been established as a high-performance photocatalyst. Historically, Sayama and Arakawa[11] were the first to observe photocatalytic performance of pristine $ZrO_2$ reporting a rather symbolic $H_2$-production yield 72 μmol $g^{-1}$ $h^{-1}$ under X-ray irradiation.

Strategies to ameliorate photocatalytic $ZrO_2$ activity, can include: (i) heteroatom insertion[12–17] into $ZrO_2$ crystal, or (ii) Oxygen-defects' creation[18–23]. The influence of heteroatoms in $ZrO_2$ has been investigated[12–17], in photocatalytic dye degradation or $O_2$ evolution. Cerium-doped $ZrO_2$ (Ce-$ZrO_2$) can be photoactive in visible $\lambda > 420$ nm light[12]. Erbium-doped $ZrO_2$[14] allowed band-gap tuning towards solar photons, which contributed to improved Methylene-Blue degradation[13]. Nitrogen[15] and carbon[17] 2p-orbitals can enhance photocatalytic dye degradation via generation of intra-bandgap states. However, in all aforementioned cases, the reported

[1]Laboratory of Physical Chemistry of Materials and Environment, Department of Physics, University of Ioannina, Ioannina, Greece. [2]Laboratory of Biomimetic Catalysis and Hybrid Materials, Department of Chemistry, University of Ioannina, 45110 Ioannina, Greece. [3]Institute of Engineering Materials and Biomaterials, Silesian University of Technology, 18a Konarskiego St, 44-100, Gliwice, Poland. [4]Institute of Environment and Sustainable Development, University Research Center of Ioannina, 45110 Ioannina, Greece. ✉email: ideligia@uoi.gr

photocatalytic performances, despite improvement, remain by far inferior versus benchmark photocatalysts, such as $TiO_2$ which routinely achieves $H_2$ photoproduction of the order of several (millimoles $H_2$ $g^{-1}$ $h^{-1}$) in typical lab set ups[24]. So far, the only $ZrO_2$-based photocatalyst passing the threshold of (millimoles $g^{-1}$ $h^{-1}$) is 2.12 mmol $H_2$ $g^{-1}$ $h^{-1}$ by a N-doped $ZrO_2$[25].

Without heteroatom doping, generation of reduced states in reducible metal-oxides, such as $TiO_2$, are decisively beneficial for $H_2$ photo yield. Examples include the work of Mao et al.[23], Naldoni et al.[26] and our Flame Spray Pyrolysis (FSP)-made black $TiO_{2-x}$[27]. $ZrO_2$ is a notoriously non-reducible oxide[28,29], since introduction of Vo's into the $ZrO_2$ lattice is not favored energetically[8,15–20], thus specific synthesis methods are needed to achieve reduction of the $ZrO_2$ lattice. To this direction, the most significant performance has been reported by Sinhamahapatra et al.[22] and Zu et al.[30], where defect-rich $ZrO_{2-x}$ has achieved production of ~ 0.5 mmol$g^{-1}$ $h^{-1}$ $H_2$ in both cases, however, this is still significantly below that of $TiO_2$[26,31].

Regarding material synthesis, none of the so far reported $ZrO_{2-x}$ synthesis methods were designed to be scalable at industrial level. Specifically, previous $ZrO_{2-x}$ synthesis methods include sol-gel[19], hydrothermal[20], high pressure/temperature processing[18,21]. More efficient methods able to overcome the non-reducibility of $ZrO_2$ are magnesiothermic[22], titaniothermic[23] and lithiothermic reduction[30] where an elementary heterometal $M^0$ atom, i.e. $Li^0$, $Ti^0$, $Mg^0$, is used to reduce $ZrO_2$ and create the desired Vo at high yield. However, all aforementioned synthesis routes include multiple steps and do not always allow facile/reproducible control or tailoring of Vo placement and populations. Particularly, the methods which require heterometal contact on $ZrO_2$ surface e.g. magnesiothermic, rely on harsh acid washes for removing the leftover hetero-metal oxide, something that mounts questions on how this may impact the state of the catalyst itself[22].

Herein we have developed a one-step Flame Spray Pyrolysis (FSP) process for synthesis of solar-light active nano-$ZrO_{2-x}$ via engineering of lattice-vacancies, Vo. FSP is eminently suited for synthesis of high crystallinity nano-$ZrO_2$[32,33], however, the synthesis of $ZrO_{2-x}$ has not been reported by FSP. In principle, $ZrO_2$ can possess two families of reduced states: (i) reduced $Zr^{3+}$ centers, and (ii) oxygen vacancies not-located on Zr atoms (Vo's). Over last decades, Giamello's group[34] has provided valuable insights into the complexity of these reduced states. Using Electron Paramagnetic Resonance (EPR) spectroscopy, in combination with quantum chemical calculations[34], they prove that $Zr^{3+}$ centers can create extra energy states right below the $E_{CB}$ of pristine $ZrO_2$, (~ 4.5–5.0 eV). Based on all existing evidence, these $Zr^{3+}$ centers are expected to have little effect on the photocatalytic activity of zirconia[35]. On the other hand, Vo's can create mid-gap states[34] but their role in photocatalytic $H_2$ evolution has not been explored systematically. Herein, using FSP we have produced libraries of $ZrO_{2-x}$ nano catalysts with varying concentrations of Vo's and identified the optimal configuration, towards high photocatalytic $H_2$-production efficiency from $H_2O$. Specific aims of the present work were: (i) to develop a novel industrial-scale FSP method for one-step synthesis of nanosized $ZrO_{2-x}$ with controllable population and placement of the O-vacancies (Vo's). No heteroatoms were used. (ii) to optimize the $ZrO_{2-x}$ for highly efficient solar light $H_2$ production, well beyond the current state of the art, i.e., well-above the threshold mmol $g^{-1}$ $h^{-1}$, (iii) to provide a comprehensive understanding of the physicochemical role of Vo, with emphasis on monomeric versus clusters of Vo's related to the photocatalytic properties. We present a novel anoxic-FSP process that allows *in-situ* formation of Vo's during the primary particle formation step. Using solar photons, the optimal nano-$ZrO_{2-x}$ can achieve milestone $H_2$-production yield, > 2400 μmol$g^{-1}$ $h^{-1}$ which is the closest so far to high photocatalytic performance benchmarks. We demonstrate that optimal nano-$ZrO_{2-x}$ can be achieved by controlling the monomeric Vo versus clusters of Vo's by two routes either during the FSP synthesis or via a short post-FSP oxidation process.

## Results

**Synthesis of nano $ZrO_{2-x}$ by anoxic-flame spray pyrolysis.** The concept of the novel anoxic-FSP process is outlined in Fig. 1. It consists of a single-nozzle FSP reactor with enclosed flame, where a mixture of Dispersion-gas [$O_2$ and $CH_4$] is used to create a reducing reaction atmosphere. In FSP-process[35], $ZrO_2$ particles are formed in three stages (Fig. 1). First, Zr-precursor droplets are sprayed by the FSP nozzle and combusted to generate the primary particles (PP)[35]. Then, primary particles evolve in the high-temperature area of the flame, i.e. up to 2800 K and form nanometric $ZrO_2$ particles via sintering of PP's[35]. In classical-FSP, used in the majority of lab studies and industry, pure $O_2$ is used as dispersion gas through the spray nozzle, to form the droplets and primary particles. For example, by adjusting the combustion stoichiometry[35] ratio P/D = [fuel/dispersion $O_2$] = 3/3, we obtain fully oxidized, pristine $ZrO_2$. In our anoxic-FSP, combustion of $CH_4$ in the dispersion gas creates reducing agents which, as we show herein, can reduce the primary Zr-particle via formation of Oxygen vacancies (Vo). We also have considered the possibility of the formation of Zr-Hydride states[36], however, none of our data support this, thus we do not discuss it further.

In this way, we have produced a library of $ZrO_{2-x}$ nanoparticles of varying Vo concentrations, see photos in Fig. 2. Herein we have codenamed the particles according to the dispersion [$O_2$/$CH_4$] ratio used, (see full details in Table S1 in SI). For example, the material codenamed [3/0.1] has been synthesized using a dispersion gas-mixture of [$O_2$ flow = 3.0 lt $min^{-1}$ and $CH_4$ flow = 0.1 lt $min^{-1}$]. Pristine $ZrO_2$ is codenamed F.O. for Fully Oxidized, while material [1.3/1.7] was the most reduced. As shown in Fig. 2, going from pristine $ZrO_2$ (F.O.) towards more reduced particles, i.e. [3/0.1] to [1.3/1.7], induced a change of particle color from crispy-white to pale grey/yellowish [3/0.1] and dark-gray for [1.3/1.7] material. XPS data (Fig. 2d) shows a progressive increase of Vo's, detected by their characteristic signal at 532 eV[37,38]. We have verified that no-carbon deposition is evidenced by Raman data, (Supplementary Fig. S1), thus the observed color changes in the $ZrO_{2-x}$ materials (Fig. 2), are assigned exclusively to the formation of Vo's via the anoxic-FSP process. According to XPS, Fig. 2d increased dispersion of the $CH_4$ in the FSP process, promotes the formation of Vo's. No $Zr^{3+}$ states are resolved in Zr-XPS data, i.e., only the $Zr^{4+}$ doublet was detected (181.9 eV, 184.2 eV) (Supplementary Fig. S2a–d).

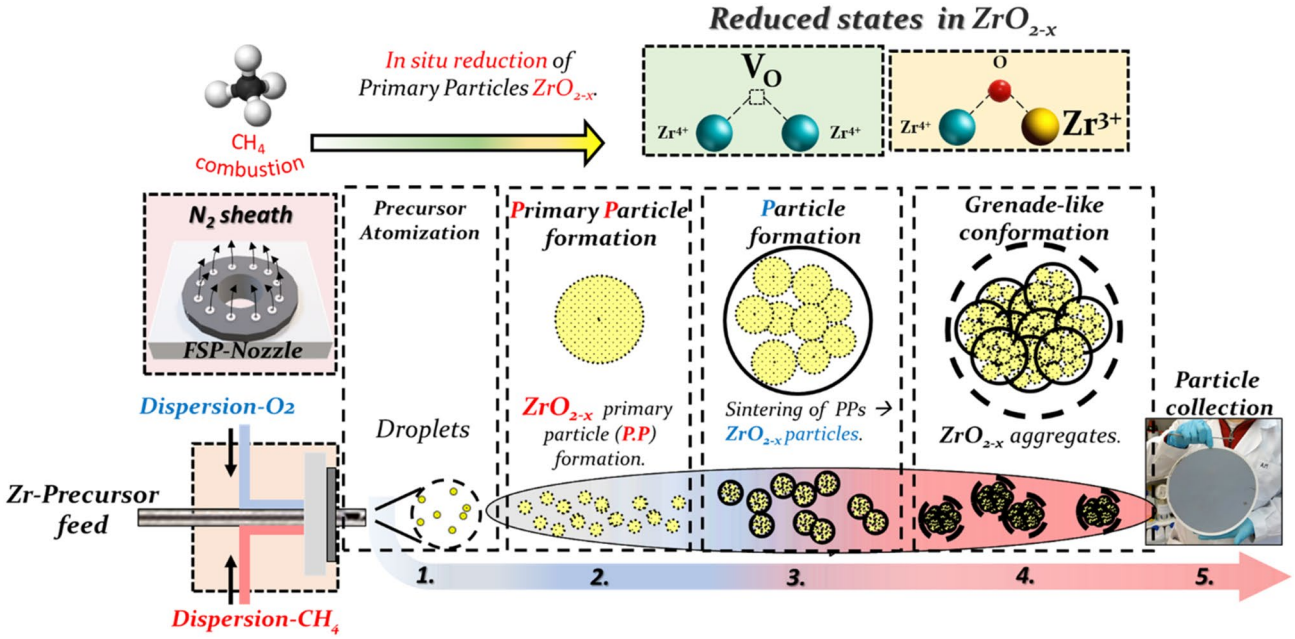


**Figure 1.** One-step FSP process for $ZrO_{2-x}$ production. The photo at right shows as-produced 500 mg of [1.3/1.7] $ZrO_{2-x}$ particles.

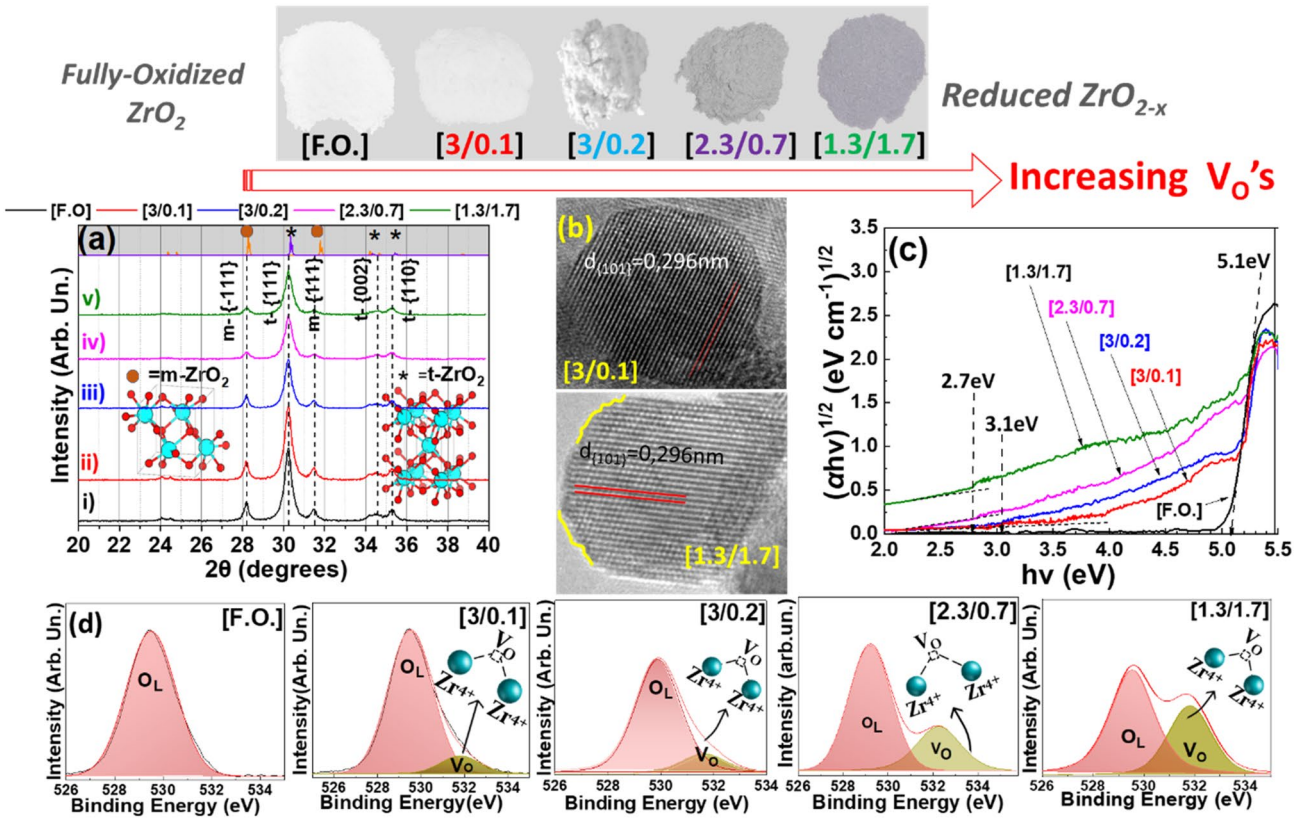


**Figure 2.** (**a**) XRD of FSP-made $ZrO_{2-x}$ materials, (**b**) TEM images for [3/0.1] and [1.3/1.7] materials, (**c**) Kubelka–Munk plots DRS UV–Vis spectra. (**d**) XPS spectra of F.O., [3/0.1], [3/0.2], [2.3/0.7] and [1.3/1.7]. *Top-Inset*: Photos of the nanopowders.

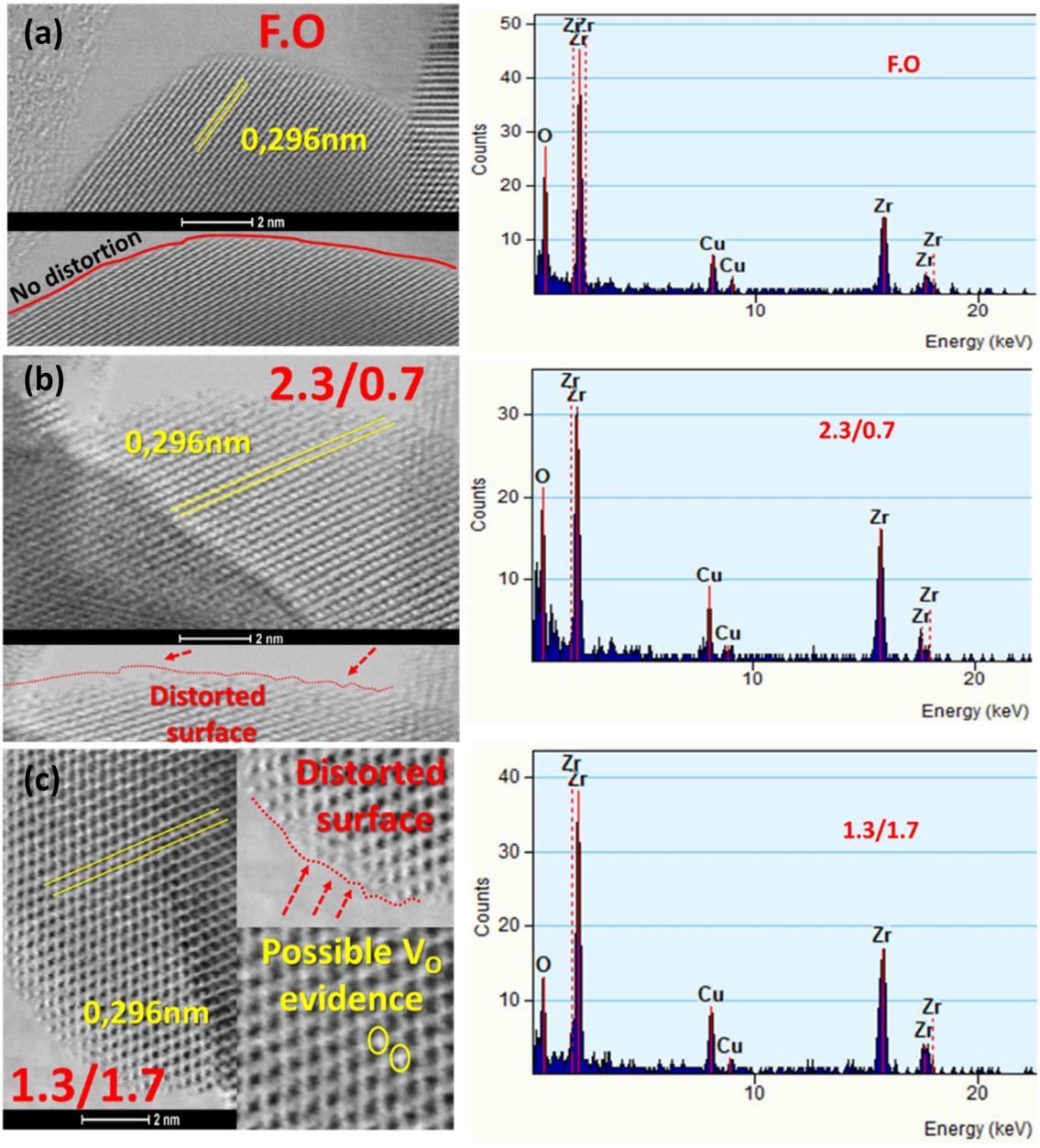


**Figure 3.** STEM images and EDX spectra of (**a**) F.O. (**b**) 2.3/0.7 and (**c**) 1.3/1.7 materials.

The DRS-UV/Vis data, (Fig. 2c) show a progressive alteration of the band gaps as evidenced by the absorbance at intra-gap energies of 2.5 to 4.5 eV. All materials exhibit the primary bandgap 5.1 eV (243 nm) typical for monoclinic-$ZrO_2$[18,20]. Fully oxidized $ZrO_2$ exhibited only the primary bandgap at 5.1 eV with no mid-gap states. Slightly-reduced [3/0.1] exhibited an additional absorbance tail band extending to ~ 3.1 eV. Low concentration of Vo's, created by 0.1 $Lmin^{-1}$ $CH_4$, (see XPS data Fig. 2d) [3/0.1], allows absorbance of photons near the middle of the primary bandgap, and creates a pale-yellow color, see photo Fig. 2. Increasing dispersion $CH_4$ (materials [3/0.2], [2.3/0.7], [1.3/1.7]) causes a monotonous enhancement of the intra-band absorbances and grey-color intensification (Fig. 2c). Experimentally[18,20,22,23,30] and theoretically[29,34] the intra-band absorbances in the range of 2.8–3.5 eV, can be assigned to electrons being injected from the $VB_{maximum}$ to approximately the middle of the gap, where extra DOS are made available through the introduction of Vo's. For example, by removing one oxygen atom, a doubly occupied (diamagnetic) F-center[39] can be created inside the bandgap $ZrO_{2-x}$ at 3.3 eV[39].

**Structural characterization.** XRD (Fig. 2a) shows that our FSP-made Zr-particles consisted of monoclinic ($m$-$ZrO_2$ in Fig. 2a) and tetragonal ($t$-$ZrO_2$ in Fig. 2a) phases, at a ratio [t-$ZrO_2$]: [m-$ZrO_2$] = 4:1 and particle sizes 22–29 nm (monoclinic) to 16–20 nm (tetragonal phase) (Table S2). At ambient P, T, $ZrO_2$ has monoclinic (m) structure with $Zr^{4+}$ atoms sevenfold coordinated by O-anions (space group $P2_1/c$). TEM images, (Figs. 2b, 3), show that all $ZrO_{2-X}$ nanomaterials have quasi-spherical shapes, with highly crystalline Miller planes $t$-{101}.

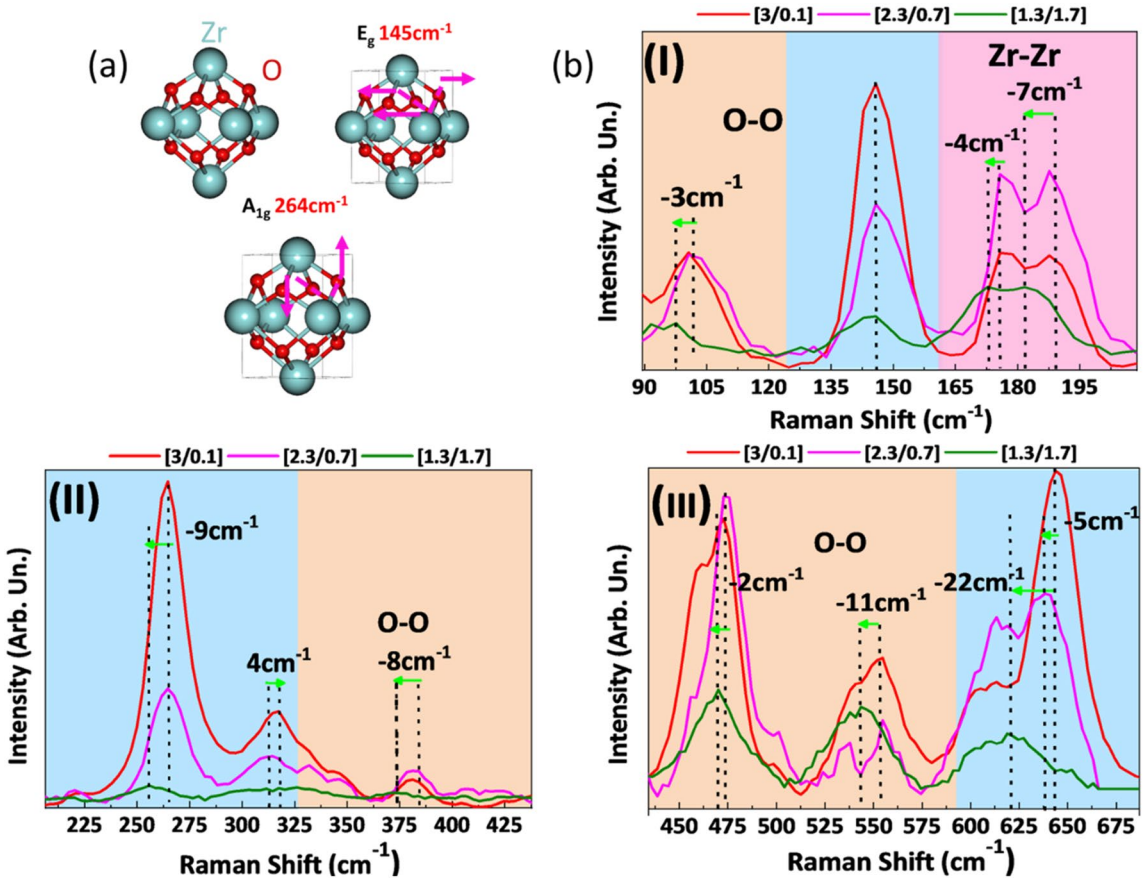


**Figure 4.** (**a**) Unit cell of $ZrO_2$with two indicative t-$ZrO_2$ lattice vibrations and (**b**) Raman downshifts in reduced $ZrO_{2-x}$.

The more reduced $ZrO_{2-X}$ nanomaterials show some degree of surface distortion, see Fig. 2b. STEM images (Fig. 3a–c) indicate that the particles retain a high degree of crystal quality even at the more reduced ones. In some cases, formation of vacancies could be evidenced in the STEM images, (Fig. 3c). EDX data (Fig. 3) confirm a strong decrease of the Oxygen/Zr ratio in the more reduced [2.3/0.7] and [1.3./1.7] materials. BET analysis (Table S2) shows progressive SSA-decrease upon increase dispersion-$CH_4$, attributed to increased aggregation of the particles at increased $CH_4$, i.e. methane creates hotter flames i.e. methane heat of combustion = 50–55 MJ/kg (https://webbook.nist.gov/chemistry/).

Raman spectra (Fig. 4b) exhibit the vibrational modes from both monoclinic and tetragonal crystal phases[40–43] (Fig. S4 and Table S3) and absence of carbon peaks (Fig. S1). In $ZrO_{2-x}$ materials, certain Raman modes are shifted (see Fig. 4b(I–III) and Table S4). More particularly, material [3/0.1] exhibits upshift of + 4 cm$^{-1}$ at 313 cm$^{-1}$ mode (Table S4). Material [2.3/0.7] exhibits downshifts of − 5 cm$^{-1}$, − 2 cm$^{-1}$, − 4 cm$^{-1}$ at 313 472 cm$^{-1}$, and 643 cm$^{-1}$ respectively (Table S4). Material [1.3/1.7] exhibits downshift of up to 22 cm$^{-1}$. Such downshifts can be attributed to tensile stress[44] effectively lengthening the bonds, see Fig. 4a, i.e. due to loss of oxygen atoms from the lattice. Raman downshifts prevail in the *t*-$ZrO_2$ phase; thus, the tetragonal phase is more responsive in the reductive atmosphere in anoxic-FSP. This can be explained by the existence of two different/non-equivalent Zr-O bond conformations in *t*-$ZrO_2$[44] corresponding to 4-coordinated Zr($O_{4f}$), and 3-coordinated Zr atoms ($O_{3f}$) respectively[44]. For comparison, the *t*-$ZrO_2$ matrix consists solely of $O_{4f}$ Zr atoms while the m-$ZrO_2$ matrix consists of both $O_{4f}$ and $O_{3f}$[44]. Accordingly, the present Raman data indicate that removal of oxygen from the $ZrO_2$ matrices is also non-equivalent, thus is easier to extract oxygen from an $O_{4f}$ site rather than an $O_{3f}$ site by 0.1 eV[22], therefore it is easier to reduce *t*-$ZrO_2$.

**Photocatalytic $H_2$ production at (millimole gr$^{-1}$ h$^{-1}$).** Figure 5a presents the photocatalytic $H_2$ production from $H_2O$, for all our $ZrO_{2-x}$ materials, under Xenon-illumination. In each panel in Fig. 5a the as-prepared photocatalysts are marked as "a.p". The time indication in each bar, refers to the post-FSP oxidation-time at 400 °C (see also XRD data in Fig. S3 in S.I.). First, we discuss the as-prepared $ZrO_{2-x}$ materials i.e., see the first bar in each column group in Fig. 5a. Pristine, (F.O.) $ZrO_2$ was practically non-photoactive in $H_2$ production, with a yield of 20 μmol g$^{-1}$ h$^{-1}$.

In contrast, a slightly reducing FSP atmosphere, i.e., as-prepared [a.p. 3/0.1], enables an impressive amelioration of $H_2$ evolution of 1700 μmol g$^{-1}$ h$^{-1}$. This demonstrates that anoxic-FSP can provide as-prepared $ZrO_{2-x}$ material exhibiting millimoles per gram per hour $H_2$ production. Further increase of $O_2/CH_4$ ratio impacted negatively the $H_2$ photogeneration with a tendency towards a steady production near 500 μmol g$^{-1}$ h$^{-1}$ of $H_2$ for

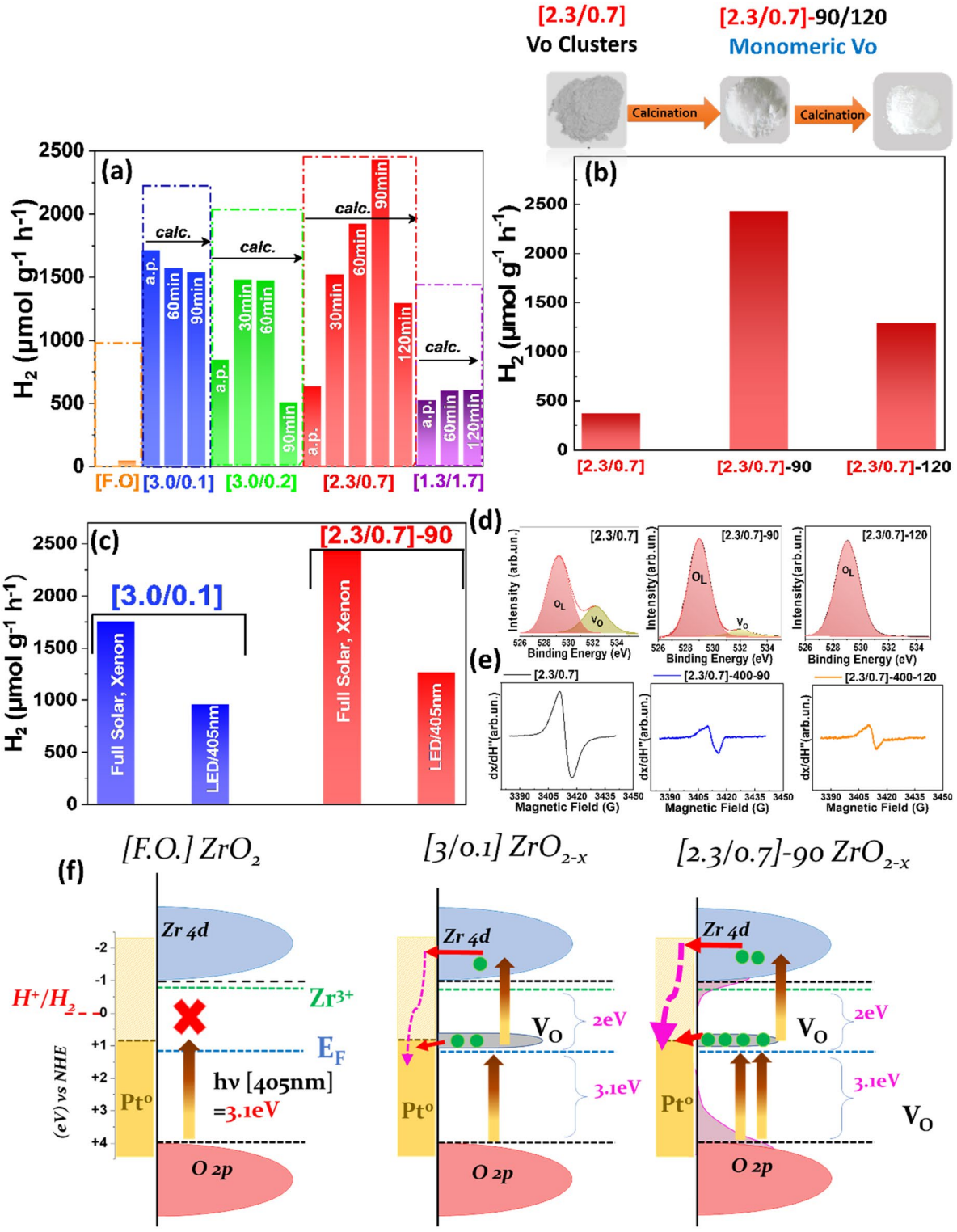


**Figure 5.** (**a**) Photocatalytic $H_2$ production from $H_2O$, by as-prepared and oxidized $ZrO_{2-x}$ catalysts under full-solar Xenon-light irradiation. (**b**) $H_2$ production by [2.3/0.7] $ZrO_{2-x}$ catalyst under various oxidation times (400 °C). (**c**) Comparison of photocatalytic $H_2$ production by the best performing $ZrO_{2-x}$ catalysts under full-solar Xenon-light versus visible 405 nm LED irradiation. (**d**) XPS spectra, (**e**) EPR spectra, indicating the evolution of the Vo's under oxidation of [2.3./0.7] $ZrO_{2-x}$. (**f**) Schematic DOS configuration and excitation under visible 405 nm, see full DFT data in S.I. Fig. S10.

the highly reduced as-prepared materials (see the first bar in each group in Fig. 5a). Soft oxidation by calcination at 400 °C under ambient $O_2$, exerted a dramatic influence on the $H_2$-photoproduction: a characteristic bell-shaped dependence was observed for the [3.0/0.2] and [2.3/0.7] materials. The optimum oxidation time was 90 min for [2.3/0.7] $ZrO_{2-x}$ which, achieved a remarkable yield of 2428 μmol $H_2$ $g^{-1}$ $h^{-1}$. The best performance of the [3.0/0.2] $ZrO_{2-x}$ material was 1500 μmol $H_2$ $g^{-1}$ $h^{-1}$ (Fig. 5a). Table S5 summarizes a comparison of FSP-$ZrO_{2-x}$ versus other pertinent $ZrO_{2-x}$ materials reported in the literature (see also Fig. S7).

The catalyst with the higher $H_2$ yield, [2.3/0.7]-90, is highly recyclable, (Fig. S5a), retaining 100% of its activity after two reuses and > 96% after four reuses. XRD (Fig. S5b), shows that the [2.3/0.7]-90 crystal remains intact after 4-uses. Concurrently, DRS-UV/Vis (Fig. S5c), demonstrates that its light-absorbance profile remains also intact. As we discuss hereafter, optimization of monomeric Vo-concentration is determinant for photocatalytic activity. In [2.3/0.7]-90, the monomeric Vo's is optimized, see EPR and XPS data in Figs. 5d,e, and S6a,b see also the trends in XPS, EPR for [2.3/0.7] in Fig. 5d,e. After photocatalytic use of [2.3/0.7]-90 material, the monomeric vacancies are not altered, neither the $ZrO_{2-x}$ crystal. Thus, the $ZrO_{2-x}$ provide a robust reusable photocatalyst.

## Discussion

The data in Fig. 5a demonstrate that there are two options to achieve high-photocatalytic performance $ZrO_{2-x}$ materials: either (i) to be prepared at low $O_2/CH_4$ ratio e.g. [3.0/0.1], or (ii) after a soft post-FSP oxidation of more reduced materials e.g. [2.3/0.7]. Very-high $O_2/CH_4$ ratio [1.3/1.7] results in highly-reduced $ZrO_{2-x}$ which cannot be improved by post-FSP oxidation.

The origins of these trends can be understood by considering the types and populations of the Vo's in $ZrO_{2-x}$. Figure 5b,d,e indicate a correlation of the $H_2$ production rates for the [2.3/0.7] $ZrO_{2-x}$ catalysts, with the Vo's detected by XPS, Fig. 5d, and EPR Fig. 5e. The XPS and EPR data show a clear decrease in the population of Vo's of the [2.3/0.7] material upon oxidation at 400 °C. Importantly, theoretical simulation of the EPR signals, Fig. 6, allows distinction between Vo-clusters versus monomeric Vo's. For example, in [a.p. 2.3/0.7] Vo clusters prevail, while in [3.0/0.1], monomeric Vo's prevail, as we can see from percentages in Fig. 6c. Oxidation progressively eliminates Vo clusters towards monomeric Vo's. This is also evident from the progressive elimination of the deep-grey color, and the changes in the UV–Vis spectra (Fig. S8 in SI). Taking this information into account, the bell-shaped $H_2$ production trend in Fig. 5b, indicates that a high concentration of O-vacancies, forming Vo clusters, is detrimental to the photocatalytic activity of $ZrO_{2-x}$. Fewer Vo's are better suited for optimal photocatalytic activity (see trend in Fig. 5a, for [2.3/0.7]). However, further oxidation of Vo's tends to delimit the photoactivity. This teaches us that a quantitative control of the Vo's clusters versus monomeric Vo is necessary, to achieve highly-performance photocatalytic $ZrO_{2-x}$, see full trend in Fig. 6e. We consider that this factor was also of pertinence in the magnesiothermically reduced $ZrO_{2-x}$ materials[22]. Although not noticed by these authors[22], inspection of their EPR spectra, shows that these correspond to Vo clusters, which concurs with their limited $H_2$ production of 506 μmol $H_2$ $g^{-1}$ $h^{-1}$, resembling our as-prepared [2.3/0.7] material.

The data under visible 405 nm LED irradiation (Fig. 5c), indicate that significant part of photocatalytic $H_2$ production, at least 70% versus the solar-light photons, can be excited by visible 405 nm photons (3.1 eV). Taking into account the DRS-UV/Vis data, (Fig. 2c) this can be attributed to the occurrence of the mid-gap states, (Fig. 5f). Theoretical DFT calculations (Fig. S10) show that in $ZrO_{2-x}$, few oxygen vacancies can create mid-gap states, located at energy distances around 3.0 eV[12,45] from both the VB-top and ~ 2.0 eV from the CB-bottom. Thus, in $ZrO_{2-x}$ the 3.1 eV photons (405 nm LED) are able to excite two consecutive electron transitions, (Fig. 5f). Increased anoxicity, i.e., as in material [2.3/0.7], enhances the DOS band-tailing (see S.I. Figs. S10 and 5f). This would increase the probability of two-photon electron photoexcitation via VB → Vo, and Vo → CB. These electrons are favorably transferred to the Pt particles, which act as electron collectors i.e. work function of Pt, φ = + 0.9 eV versus NHE[46], is favorable for acceptance of electrons from the highly-excited electrons in the CB.

**Quantitate analysis of $V_O$-clusters versus monomeric Vo's, by EPR and XPS.** Numerical EPR simulations, dashed lines Fig. 6a, show that monomeric Vo's were characterized by an inhomogeneous line-shape with linewidth $\Delta H_{monomer} = (9.4 \pm 0.1)$Gauss and a rhombic $g_{monomer}$-tensor, (Table S5). Vo clusters are characterized by a Lorenz line-shape and $\Delta H_{cluster} = (4.6 \pm 0.1)$ Gauss and isotropic $g_{cluster}$-tensor, (Table S6).

The structural significance of this is: for isotropic EPR signals with low g-anisotropy, a Gaussian line-shape is the fingerprint of the so-called *in*homogeneously-broadened S = 1/2 states[47,48] which is indicative of isolated Vo's, with no-interactions[47,48]. Physically, this indicates that in the $ZrO_{2-x}$ particles produced under low $CH_4$-flow e.g. [3/0.1], monomeric isolated $Vo^{EPR}$ centers. The Lorentz line-shape of the Vo clusters indicates that it originates from Vo centers with spin-exchange and/or fast dipolar interactions. In $ZrO_{2-x}$, this Lorentz line-shape indicates formation of Vo-clusters upon increasing dispersion-$CH_4$.

Comparing the XPS data for surface-Vo's (Fig. 6d) versus the quantitative data for total-paramagnetic Vo's, (Fig. 6c and Table S7 in SI), derived from the EPR spectra (Fig. 6b) and their deconvolution in monometer/clusters (see example for [1.3/1.7] in Fig. S9 in SI), we notice a correlation: highly reduced $ZrO_{2-x}$, have higher surface-Vo's, and total paramagnetic Vo's. Figure 6e provides an overview plot, which shows that optimization of $H_2$ photocatalysis can be achieved via optimization of $V_O$-Clusters versus monomeric Vo's by two routes: (i) control of FSP anoxicity, or (ii) by soft post-FSP oxidation. This demonstrates that our novel anoxic-FSP process allows facile synthesis of solar-light active nano-$ZrO_{2-x}$ via engineering of lattice-vacancies, Vo. Control of monomeric Vo versus clusters of Vo's is the key-parameter toward Highly-Performing-Photocatalytic $ZrO_{2-x}$. The anoxic-FSP process presented here, should be easily adaptable to existing industrial-scale FSP reactors. This offers an efficient technology that can be adopted in the future and provide new tools for the design of other families of photoactive nanomaterials via control of oxygen vacancies.

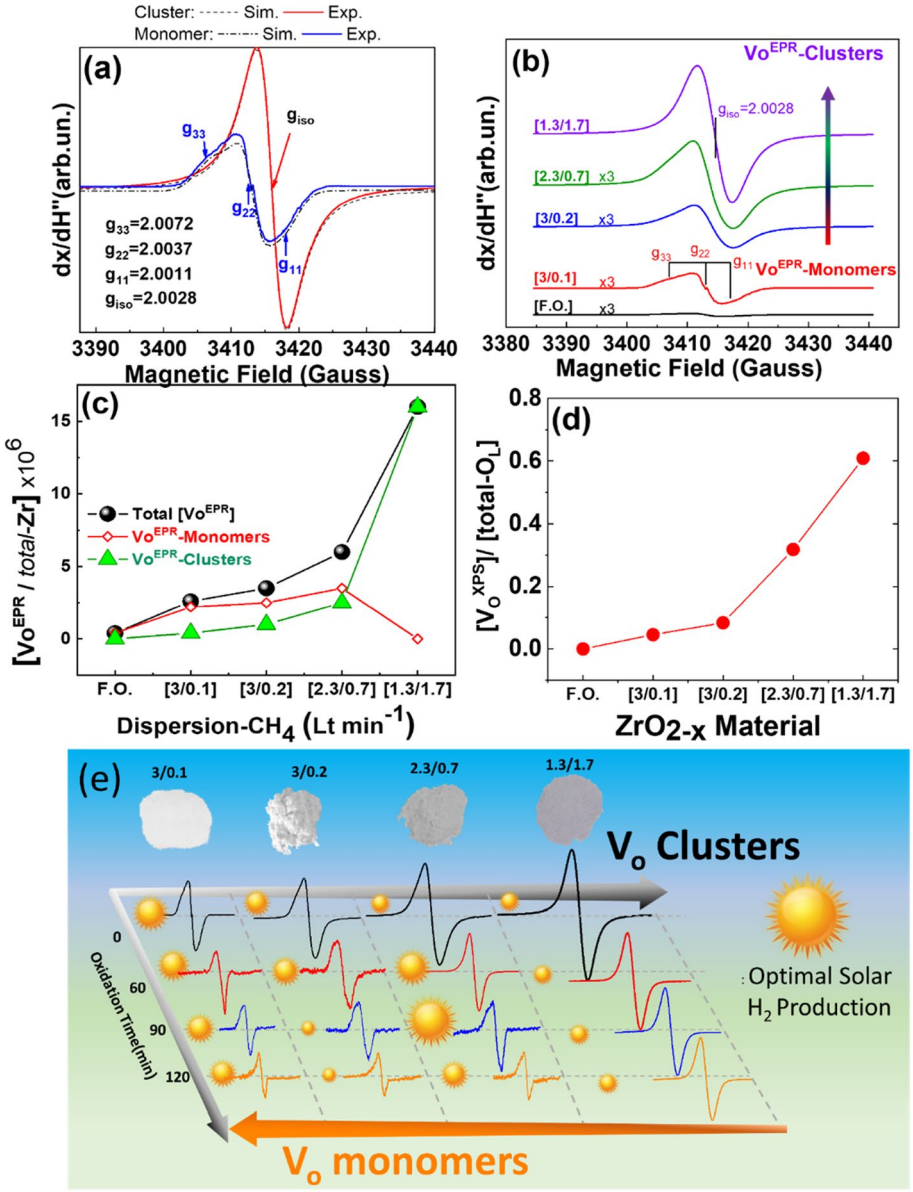


**Figure 6.** (**a**) Experimental (solid-lines) and theoretical EPR (dashed-lines) spectra of Vo's formed in as-prepared [3/0.1] $ZrO_{2-x}$ (blue, monomeric Vo's) or [1.3/1.7] $ZrO_{2-x}$ (red, Vo clusters) (**b**) Experimental EPR spectra, showing the progressive transition from pure-monomeric Vo's in [3/0.1] $ZrO_{2-x}$ towards Vo-clusters in [1.3/1.7] $ZrO_{2-x}$ (**c**) Ratio of EPR detectable oxygen vacancies $V_O^{EPR}$ over total Zr-atoms present in each $ZrO_{2-x}$ material (**d**) Ratio of $Vo^{XPS}$ determined by XPS over total oxygen atoms in the lattice. (**e**) Control of (Monomeric Vo/Vo Cluster) ratio in as-prepared $ZrO_{2-x}$ or via post-FSP oxidation, allows optimization of the photocatalytic $H_2$ production. The size of the sun-symbol exemplifies the $H_2$ production efficiency.

## Methods

**Synthesis of nanomaterials by FSP.** Precursor solution was prepared by dissolving Zirconium (IV) Propoxide (70 wt% in 1-propanol) in xylene and acetonitrile in a 2.2/1.0 ratio at a concentration of 0.25 M. Then, the solution was fed through a capillary at 3 ml $min^{-1}$ and dispersed to a self-sustained oxygen/methane (4–2 L $min^{-1}$) pilot flame to initiate combustion. An important distinction must be made which leads to the innovation of the presented work. $ZrO_{2-x}$ materials were prepared by modifying the dispersion feed. While keeping the 3 ml $min^{-1}$ dispersion constant, methane gas ($CH_4$) was fed along with the traditional dispersion gas ($O_2$). The resulting high temperatures and hydride formation through the decomposition of methane lead to the formation of $ZrO_{2-x}$. Furthermore, the protocol of methane injection ensures the formation of bulk defects as the particle is influenced at its early stages of flight, at the primary particle stage. Finally, the pressure drop was fixed at 1.5–2.0 bar, and an additional 10 L $min^{-1}$ $O_2$ sheath was used to aid in particle collection which was made possible by a vacuum pump (Busch V40) and by a glass microfiber filter (GF 6 257, Hahnemühle, Dassel, Germany).

**Characterization techniques.** Powder X-Ray Diffraction (XRD) data were collected at room temperature using a Bruker D8 Advance 2theta diffractometer with copper radiation (Cu Ka, λ = 1.5406 Å) and a secondary monochromator operating at 36 kV and 36 mA. Crystal size is calculated by the Scherrer formula. X-Ray photoelectron spectroscopy (XPS) data were collected by a surface analysis ultrahigh vacuum system (SPECS GmbH) equipped with a twin Al–Mg anode X-ray source and a multichannel hemispherical sector electron analyzer (HSA Phoibos 100). The base pressure was $2-5\times10^{-9}$ mbar. A monochromatized Mg Kα line at 1253.6 eV and analyzer pass energy of 20 eV were used in all XPS measurements. The binding energies were calculated with reference to the energy of $C_{1s}$ peak of contaminant carbon at 284.5 eV. The peak deconvolution was calculated using a Shirley background.

Raman HORIBA-Xplora Plus spectrometer, equipped with an Olympus BX41 microscope. A 785 nm diode laser was used as an excitation source, and the laser beam was focused on the sample with the aid of the microscope. Before measurement, each powder material was softly pressed between two glass plates to form a pellet-like structure. Brunauer–Emmett–Teller (BET) adsorption–desorption isotherms were recorded at 77 K using a Quantachrome NOVA touch $LX^2$. Outgassing was performed at 80 °C for 5 h under vacuum, before the measurements. The absorption data points in the relative pressure $P/P_o$ range of 0.1–0.3 was used to calculate the specific surface area (SSA).

**Electron paramagnetic resonance spectroscopy.** The X-band electron paramagnetic resonance (EPR) spectra of $ZrO_2/ZrO_{2-x}$ materials were recorded with a Bruker ER200D spectrometer at 77 K, equipped with an Agilent 5310A frequency counter. The spectrometer was running under a custom-made software based on LabView. Adequate signal-to-noise ratio was obtained after 15–20 scans, with a microwave power fixed at 20 mW. The EPR instrumental conditions were as follows: microwave frequency = 9.53 GHz and modulation amplitude = 10 Gpp.

**Theoretical analysis of the EPR spectra.** The experimental EPR spectra were simulated using the EasySpin software. A S = 1/2 Spin Hamiltonian was used $\hat{H} = \beta\vec{B}\cdot g\cdot\vec{S}$ where β is the Bohr magneton, $\vec{B}$ is the applied magnetic field, g is the spectroscopic g-tensor and $\vec{S}$ the spin angular momentum. The X-band electron paramagnetic resonance (EPR) spectra were recorded with a Bruker ER200D spectrometer at 77 K, equipped with an Agilent 5310A frequency counter. The spectrometer was running under a home-made software based on LabView. Adequate signal-to-noise ratio was obtained after 30–50 scans. The EPR instrumental conditions were as follows: microwave frequency = 9.55 GHz, modulation frequency = 50.00 kHz, and modulation amplitude = 10 Gauss peak-to-peak.

**Photocatalytic $H_2$ evolution procedure.** The photocatalytic hydrogen reactions were realized into a double wall Pyrex reactor, cooled with tap circulation (T = 25 °C). Light source was a Solar Simulator, (Sciencetech, Class AAA, model SciSun-150) with average irradiation intensity of 180 W $m^{-2}$ equipped with a xenon lamp of 150 W and Air Mass filter (1 sun, AM1.5G). As Visible light source was used a Led lamp FireEdge™ FE410 (λ = 405 nm) supplied by Phoseon company, which power intensity was set to be 180 W $m^{-2}$, using a power meter (Thorlabs Inc., USA). In each experiment, 50 mg of the catalyst was suspended into 150 ml water/methanol mixture 20% v/v (final concentration of the catalyst 330 mg $L^{-1}$). Atmospheric $O_2$ from the suspension was removed, fulfilling the content of reactor with Ar gas (99.9997%) at least 1 h. As Pt source were used the dihydrogen hexachloroplatinate (IV) hydrate complex ($H_2Pt_4Cl_6$. $6H_2O$, 99.99%, Alfa Aesar) which was photodeposited in situ, at the reaction mixture. Qualitative and quantitative monitoring of produced $H_2$ and $CO_2$ gases was done via a continuous online GasChromatography System combined with a Thermo-conductive Detector (GC-TCD- Shimadzu GC-2014, carboxen 1000 column, Ar carrier gas[49].

**Post-FSP oxidation.** A ThermaWatt furnace was used, equipped with a tubular Quartz compartment[50]. Oxidations were performed under atmospheric $O_2$ at temperature 400 °C and calcination time was varied from 30 to 120 min through intervals of 30 min.

## Data availability

All data generated or analysed during this study are included in this published article (and its supplementary information files).

Received: 8 June 2022; Accepted: 29 August 2022
Published online: 07 September 2022

## References

1. Hwang, J. *et al.* Perovskites in catalysis and electrocatalysis. *Science* **358**, 751–756 (2017).
2. Seh, Z. W. *et al.* Combining theory and experiment in electrocatalysis: Insights into materials design. *Science* **355**, 4998 (2017).
3. Fang, H. Challenges with the ultimate energy density with Li-ion batteries. *IOP Conf. Ser. Earth Environ. Sci.* **781**, 042023 (2021).
4. Villa, K., Galán-Mascarós, J. R., López, N. & Palomares, E. Photocatalytic water splitting: Advantages and challenges. *Sustain. Energy Fuels* **5**, 4560–4569 (2021).
5. Singh, N., Prakash, J. & Gupta, R. K. Design and engineering of high-performance photocatalytic systems based on metal oxide–graphene–noble metal nanocomposites. *Mol. Syst. Des. Eng.* **2**, 422–439 (2017).
6. Aksel, C. The microstructural features of an alumina–mullite–zirconia refractory material corroded by molten glass. *Ceram. Int.* **29**, 305–309 (2003).
7. Clarke, D. R., Oechsner, M. & Padture, N. P. Thermal-barrier coatings for more efficient gas-turbine engines. *MRS Bull.* **37**, 891–898 (2012).

8. Radhakrishnan, J. K., Kamble, S. S., Krishnapur, P. P., Padaki, V. C. & Gnanasekaran, T. Zirconia Oxygen Sensor for aerospace applications. In *2012 Sixth International Conference on Sensing Technology (ICST)* 714–717 (IEEE, 2012). https://doi.org/10.1109/ICSensT.2012.6461771
9. Dhanasekaran, P., Williams, S. R., Kalpana, D. & Bhat, S. D. Boosting efficiency and stability using zirconia nanosphere-held carbon for proton exchange membrane fuel cells. *RSC Adv.* **8**, 472–480 (2018).
10. Jeong, D.-W., Na, H.-S., Shim, J.-O., Jang, W.-J. & Roh, H.-S. A crucial role for the $CeO_2$–$ZrO_2$ support for the low temperature water gas shift reaction over Cu–$CeO_2$–$ZrO_2$ catalysts. *Catal. Sci. Technol.* **5**, 3706–3713 (2015).
11. Sayama, K. & Arakawa, H. Photocatalytic decomposition of water and photocatalytic reduction of carbon dioxide over zirconia catalyst. *J. Phys. Chem.* **97**, 531–533 (1993).
12. Gionco, C. *et al.* Cerium-doped zirconium dioxide, a visible-light-sensitive photoactive material of third generation. *J. Phys. Chem. Lett.* **5**, 447–451 (2014).
13. Hernández, S. *et al.* Insights into the sunlight-driven water oxidation by Ce and Er-doped $ZrO_2$. *Front. Chem.* **6**, 368 (2018).
14. Gionco, C. *et al.* Rare earth oxides in zirconium dioxide: How to turn a wide band gap metal oxide into a visible light active photocatalyst. *J. Energy Chem.* **26**, 270–276 (2017).
15. Sudrajat, H., Babel, S., Sakai, H. & Takizawa, S. Rapid enhanced photocatalytic degradation of dyes using novel N-doped $ZrO_2$. *J. Environ. Manag.* **165**, 224–234 (2016).
16. Bugrov, A. N., Rodionov, I. A., Zvereva, I. A., Smyslov, RYu. & Almjasheva, O. V. Photocatalytic activity and luminescent properties of Y, Eu, Tb, Sm and Er-doped $ZrO_2$ nanoparticles obtained by hydrothermal method. *Int. J. Nanotechnol.* **13**, 147 (2016).
17. Poungchan, G., Ksapabutr, B. & Panapoy, M. One-step synthesis of flower-like carbon-doped $ZrO_2$ for visible-light-responsive photocatalyst. *Mater. Des.* **89**, 137–145 (2016).
18. Wang, Q. *et al.* Photocatalytic hydrogen generation on low-bandgap black zirconia ($ZrO_2$) produced by high-pressure torsion. *J. Mater. Chem. A* **8**, 3643–3650 (2020).
19. Imparato, C. *et al.* Unraveling the charge state of oxygen vacancies in $ZrO_{2-x}$ on the basis of synergistic computational and experimental evidence. *J. Phys. Chem. C* **123**, 11581–11590 (2019).
20. Song, L., Cao, X. & Li, L. Engineering stable surface oxygen vacancies on $ZrO_2$ by hydrogen-etching technology: An efficient support of gold catalysts for water–gas shift reaction. *ACS Appl. Mater. Interfaces* **10**, 31249–31259 (2018).
21. Teeparthi, S. R., Awin, E. W. & Kumar, R. Dominating role of crystal structure over defect chemistry in black and white zirconia on visible light photocatalytic activity. *Sci. Rep.* **8**, 5541 (2018).
22. Sinhamahapatra, A., Jeon, J.-P., Kang, J., Han, B. & Yu, J.-S. Oxygen-deficient zirconia ($ZrO_{2-x}$): A new material for solar light absorption. *Sci. Rep.* **6**, 27218 (2016).
23. Qi, F. *et al.* Interfacial reaction-induced defect engineering: Enhanced visible and near-infrared absorption of wide band gap metal oxides with abundant oxygen vacancies. *ACS Appl. Mater. Interfaces* **12**, 55417–55425 (2020).
24. Solakidou, M., Georgiou, Y. & Deligiannakis, Y. Double-nozzle flame spray pyrolysis as a potent technology to engineer noble metal-$TiO_2$ nanophotocatalysts for efficient $H_2$ production. *Energies* **14**, 817 (2021).
25. Wang, Y. *et al.* Novel N-doped $ZrO_2$ with enhanced visible-light photocatalytic activity for hydrogen production and degradation of organic dyes. *RSC Adv.* **8**, 6752–6758 (2018).
26. Naldoni, A. *et al.* Photocatalysis with reduced $TiO_2$: From black $TiO_2$ to cocatalyst-free hydrogen production. *ACS Catal.* **9**, 345–364 (2019).
27. Fujiwara, K., Deligiannakis, Y., Skoutelis, C. G. & Pratsinis, S. E. Visible-light active black $TiO_2$–Ag/$TiO_x$ particles. *Appl. Catal. B Environ.* **154–155**, 9–15 (2014).
28. Ruiz Puigdollers, A., Schlexer, P., Tosoni, S. & Pacchioni, G. Increasing oxide reducibility: The role of metal/oxide interfaces in the formation of oxygen vacancies. *ACS Catal.* **7**, 6493–6513 (2017).
29. Pacchioni, G. Numerical simulations of defective structures: The nature of oxygen vacancy in non-reducible (MgO, $SiO_2$, $ZrO_2$) and reducible ($TiO_2$, NiO, $WO_3$) oxides. In *Defects at Oxide Surfaces* Vol. 58 (eds Jupille, J. & Thornton, G.) 1–28 (Springer International Publishing, 2015).
30. Zu, D. *et al.* Black $ZrO_2$ synthesized by molten lithium reduction strategy for photocatalytic hydrogen generation. *J. Am. Ceram. Soc.* **103**, 4035–4042 (2020).
31. Sinhamahapatra, A., Jeon, J.-P. & Yu, J.-S. A new approach to prepare highly active and stable black titania for visible light-assisted hydrogen production. *Energy Environ. Sci.* **8**, 3539–3544 (2015).
32. Mädler, L., Kammler, H. K., Mueller, R. & Pratsinis, S. E. Controlled synthesis of nanostructured particles by flame spray pyrolysis. *J. Aerosol Sci.* **33**, 369–389 (2002).
33. Stahl, J. *et al.* Comparing co-catalytic effects of $ZrO_x$, $SmO_x$, and Pt on $CO_x$ methanation over Co-based catalysts prepared by double flame spray pyrolysis. *ChemCatChem* **13**, 2815–2831 (2021).
34. Gionco, C. *et al.* Paramagnetic defects in polycrystalline zirconia: An EPR and DFT study. *Chem. Mater.* **25**, 2243–2253 (2013).
35. Koirala, R., Pratsinis, S. E. & Baiker, A. Synthesis of catalytic materials in flames: Opportunities and challenges. *Chem. Soc. Rev.* **45**, 3053–3068 (2016).
36. Weaver, J. H., Peterman, D. J., Peterson, D. T. & Franciosi, A. Electronic structure of metal hydrides. IV. TiHx, ZrHx, HfHx, and the fcc-fct lattice distortion. *Phys. Rev. B* **23**, 1692–1698 (1981).
37. Lackner, P., Zou, Z., Mayr, S., Diebold, U. & Schmid, M. Using photoelectron spectroscopy to observe oxygen spillover to zirconia. *Phys. Chem. Chem. Phys.* **21**, 17613–17620 (2019).
38. Ma, W., Herbert, F. W., Senanayake, S. D. & Yildiz, B. Non-equilibrium oxidation states of zirconium during early stages of metal oxidation. *Appl. Phys. Lett.* **106**, 101603 (2015).
39. Ricca, C., Ringuedé, A., Cassir, M., Adamo, C. & Labat, F. A comprehensive DFT investigation of bulk and low-index surfaces of $ZrO_2$ polymorphs. *J. Comput. Chem.* **36**, 9–21 (2015).
40. Quintard, P. E., Barbéris, P., Mirgorodsky, A. P. & Merle-Méjean, T. Comparative lattice-dynamical study of the Raman spectra of monoclinic and tetragonal phases of zirconia and hafnia. *J. Am. Ceram. Soc.* **85**, 1745–1749 (2004).
41. Naumenko, A. P., Berezovska, N. I., Biliy, M. M. & Shevchenko, O. V. Vibrational analysis and Raman spectra of tetragonal zirconia. *Phys. Chem. Solid State* **9**, 121–125 (2008).
42. Kim, B.-K. & Hamaguchi, H. Mode assignments of the Raman spectrum of monoclinic zirconia by isotopic exchange technique. *Phys. Status Solidi B* **203**, 557–563 (1997).
43. Hirata, T., Asari, E. & Kitajima, M. Infrared and Raman spectroscopic studies of $ZrO_2$ polymorphs doped with $Y_2O_3$ or $CeO_2$. *J. Solid State Chem.* **110**, 201–207 (1994).
44. Nye, J. F. & Lindsay, R. B. Physical properties of crystals: Their representation by tensors and matrices. *Phys. Today* **10**, 26–26 (1957).
45. Perevalov, T. V. & Islamov, D. R. Atomic and electronic structure of oxygen polyvacancies in $ZrO_2$. *Microelectron. Eng.* **178**, 275–278 (2017).
46. Tisdale, W. A. *et al.* Hot-electron transfer from semiconductor nanocrystals. *Science* **328**, 1543–1547 (2010).
47. Portis, A. M. Electronic structure of F centers: Saturation of the electron spin resonance. *Phys. Rev.* **91**, 1071–1078 (1953).
48. Castner, T. G. Saturation of the paramagnetic resonance of a V center. *Phys. Rev.* **115**, 1506–1515 (1959).
49. Solakidou, M. *et al.* Efficient photocatalytic water-splitting performance by ternary CdS/Pt-N-$TiO_2$ and CdS/Pt-N, F-$TiO_2$: Interplay between CdS photo corrosion and $TiO_2$-dopping. *Appl. Catal. B Environ.* **254**, 194–205 (2019).

50. Stathi, P., Solakidou, M. & Deligiannakis, Y. Lattice defects engineering in W-, Zr-doped $BiVO_4$ by flame spray pyrolysis: Enhancing photocatalytic $O_2$ evolution. *Nanomaterials* **11**, 501 (2021).

## Acknowledgements
This research was funded by the Hellenic Foundation for Research and Innovation (H.F.R.I) under the "First Call for H.F.R.I Research Projects to support Faculty members and Researchers and the procurement of high-cost research equipment grant" (Grant HFRI-1888).

## Author contributions
A.M.; Particle synthesis and characterization, writing-original draft, A.Z.; Particle synthesis, Writing-original draft, M.S.; Photocatalytic experiments, Writing—review and editing, S.S. TEM analysis, Y.D.; Conceptualization, Supervision, Funding acquisition, Writing—review and editing.

## Competing interests
The authors declare no competing interests.

## Additional information
**Supplementary Information** The online version contains supplementary material available at https://doi.org/10.1038/s41598-022-19382-3.

**Correspondence** and requests for materials should be addressed to Y.D.

**Reprints and permissions information** is available at www.nature.com/reprints.

**Publisher's note** Springer Nature remains neutral with regard to jurisdictional claims in published maps and institutional affiliations.